PAPER

Influence of neodymium substitution on structural, magnetic and spectroscopic properties of Ni–Zn–Al nano-ferrites

N. Amri, [ID] *[a] J. Massoudi, [ID] *[a] K. Nouri,[b] M. Triki,[c] E. Dhahri [ID] [a] and L. Bessais[b]

$Ni_{0.6}Zn_{0.4}Al_{0.5}Fe_{1.5-x}Nd_xO_4$ ferrite samples, with $x = 0.00$, 0.05, 0.075 and 0.1, were synthesized using the sol–gel method. The effects of Nd^{3+} doping on the structural, magnetic and spectroscopic properties were investigated. XRD Rietveld refinement carried out using the FULLPROF program shows that the Ni–Zn ferrite retains its pure single phase cubic structure with $Fd\bar{3}m$ space group. An increase in lattice constant and porosity happens with increasing Nd^{3+} concentration. FTIR spectra present the two prominent absorption bands in the range of 400 to 600 cm^{-1} which are the fingerprint region of all ferrites. The change in Raman modes in the synthesized ferrite system were observed with Nd^{3+} substitution. The magnetization curves show a typical transition, at the Curie temperature T_C, from a low temperature ferrimagnetic state to a high temperature paramagnetic state. The saturation magnetization, coercivity and remanence magnetization are found to be decreasing with increasing the Nd^{3+} concentration.

Introduction

Spinel ferrites AB_2O_4 have a crystal structure belonging to $Fd\bar{3}m$ space group where the tetrahedral A site is occupied by divalent metals and the octahedral B site is occupied by trivalent cations. Particularly, Ni–Zn ferrites have enormous importance in technological and scientific applications such as electrical devices, microwave industries, chemical sensors, *etc.* due to their interesting physico-chemical properties. These materials are chosen for their high resistivity, high Curie temperature, low current losses *etc.*

Several studies were done with varying the doping cations (divalent or trivalent)[1,2] and synthesizing the desired compounds with different methods such as sol–gel, thermal combustion, co-precipitation[3–6] in order to ameliorate certain structural, magnetic or dielectric properties as required in scientific and technological domains.

The magnetic and dielectric properties of Ni–Zn ferrites are controlled by the substitution of iron sites by magnetic or non-magnetic ions. The neodymium Nd which is a magnetic ion with a greater ionic radius (0.99 Å) than iron (0.67 Å) has a capability to modify the characteristics of ferrites. The doping of neodymium (Nd^{3+}) in spinel ferrites decreases the saturation magnetization, and also increases the density and resistivity of the spinel ferrite due to unpaired electrons in the 4f orbital of Nd^{3+} that give rise to ion with a nonmagnetic nature.[7] Moreover, the larger ionic radii Nd^{3+} ions replace Fe ions at the octahedral site of the ferrites which results in improved magnetic and electrical properties of the ferrites for the high-frequency application.[8–10]

X. Wu *et al.*[11] synthesized $Ni_{0.5}Zn_{0.5}Nd_xFe_{2-x}O_4$ ($0.0 \leq x \leq 0.12$) samples by calcining oxalates in air. They reported that magnetic properties were improved after doping with neodymium. P. Pranav *et al.*[12] also announced an enhancement in saturation magnetization of $Mn_{0.6}Zn_{0.4}Fe_{2-x}Nd_xO_4$ ($x = 0$, 0.04, 0.06, 0.08, and 0.1) prepared using combustion method. Moreover, Luo *et al.*[13] discussed the impact of neodymium substitution on structural, dielectric and magnetic properties of polycrystalline $Ni_{0.5}Zn_{0.5}Nd_xFe_{2-x}O_4$ ($0.002 \leq x \leq 0.010$) ferrites. They found that the mechanism of doping induced modulation on structural, dielectric and magnetic properties.

In this paper, we aim to investigate the effect of neodymium on the structural, morphological and magnetic properties of $Ni_{0.6}Zn_{0.4}Al_{0.5}Fe_{1.5-x}Nd_xO_4$ synthesized using sol–gel route. Spectroscopic properties were discussed based on FTIR and Raman measurements.

Experimental procedure

Crystal nano-particles with chemical composition $Ni_{0.6}Zn_{0.4}$-$Al_{0.5}Fe_{1.5-x}Nd_xO_4$ with $x = 0.00$, 0.05, 0.075 and 0.1 were prepared *via* sol–gel method. The starting materials used to prepare our samples are $NiCl_2 \cdot 6H_2O$, ZnO, Al_2O_3,

[a]Laboratoire de Physique Appliquée, Faculté des Sciences de Sfax, Université de Sfax, B.P. 1171, 3000 Sfax, Tunisia. E-mail: amrinoura90@gmail.com; jalel.massoudi@gmail.com

[b]ICMPE (UMR 7182), CNRS, UPEC, Université Paris Est, 94320 Thiais, France

[c]Laboratoire de Physique des Matériaux, Faculté des Sciences de Sfax, Université de Sfax, B. P 1171, 3000 Sfax, Tunisia. E-mail: mtriki_fss@yahoo.fr

$Fe(NO_3)_3 \cdot 9H_2O$ and Nd_2O_3 (all used chemicals were of analytical grade with purity $\geq$99%). The required precursors $NiCl_2 \cdot 6H_2O$ and $Fe(NO_3)_3 \cdot 9H_2O$ were taken in stoichiometric amounts and were dissolved in distilled water to obtain a mixed solution. The oxides powders ZnO, Al_2O_3 and Nd_2O_3 were dissolved in nitric acid thenjoinedto the solution drop by drop. Next, ethylene glycol ($C_2H_6O_2$)was added to the mixture as a complexing agent in order to get transparent solution with homogenous distribution of metal ionsafter adding the citric acid (molar ratio 1 : 1.5 of metal cation (Ni + Fe + Zn + Al + Nd) to citric acid). Using a hot plate magnetic stirrer, the mixture was stirred at 80 °C during 6 hours. After that, the viscous solution gets converted into a homogenous brown gel then to a powder. The burned gel was ground to get a fine ferrite powder by using an agate mortar. The powder were annealed at 500 °C for 6 hours in an electrical muffle furnace and cooled slowly in room temperature to decompose the organic matter. Finally, the obtained powder was pelletized and annealed at 900 °C during 6 hours.

Characterizations

In order to identify the crystal phase formation of our materials, we used the X-ray diffraction (XRD) patterns which were recorded on a Bruker D8 powder X-ray diffractometer using the Cu (Kα) radiation ($\lambda = 1.5406$ Å)with a step size of 0.015° for 13.5 s over a 2 h range from 15° to 80°. The morphological study was performed by Merlin Scanning Electron Microscopy (SEM) equipped with an energy-dispersive X-ray spectrometer (EDXS). Fourier transform infrared (FTIR) spectroscopy of synthesized samples was used to find the functional groups and vibrational structure on the surface, within Thermo Scientific Nicolet 6700 FTIR Spectrometer in the region 400–4000 cm^{-1} at room temperature with diffuse reflectance infrared Fourier transform spectroscopy (DRIFTS) technique. Raman scattering measurements were performed using a SENTERRA spectrometer (Bruker, Germany) with laser excitation of 532 nm at room temperature. Magnetic measurements of magnetization *versus* temperature for all ferrites samples were carried out using differential sample magnetometer MANICS in a field up to 16 kOe. Hysteresis loops of the present ferrites have been traced using a SQUID magnetometer under magnetic field up to 4 T, at room temperature.

Results and discussion

Structural study

Fig. 1 presents the X-ray diffraction pattern of Ni–Zn–Al ferrite samples recorded in the 2θ range between 10° and 80°. The Rietveld refinements of these patterns show that all samples crystallize in the cubic structure with $Fd\bar{3}m$ space group. The essential reflection peaks were from the characteristic crystal planes of cubic single phase spinel structure (111), (220), (311), (222), (400), (422), (511), (440), (620) and (533).[14–16] It can be observed from Fig. 1, the existence of extra peaks for $x = 0.1$ sample which refers to orthorhombic ferrite symmetry *Pbnm* as a second phase ($NdFeO_3$) symbolized by (*). The orthorhombic
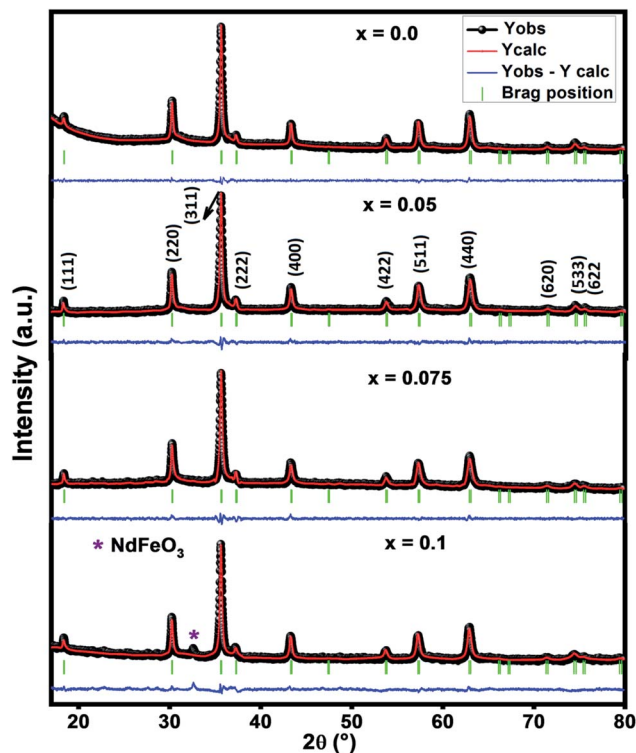

Fig. 1 Rietveld analysis of X-ray powder diffraction pattern of Ni–Zn ferrites.

ferrite phase has been also observed in the literature.[17,18] However, the small amount of Nd^{3+} ions in Ni–Zn–Al ferrite can affect not only the phase composition but also the size of the spinel matrix, which is due to orthoferrite ($NdFeO_3$) phase. Pawar *et al.*[18] reported that the most important reason for the orthorhombic phase formation in the rare earth element substituted spinel ferrites is the electronic configuration, larger ionic radii of rare earth element and diffusion of rare earth ions at the grain boundaries. It is worth to mention here that, up to $x = 0.075$, Nd^{3+} is highly soluble in Ni–Zn–Al ferrite. This level of Nd^{3+} solubility is quite better as compared to previous reports related to rare earth doping.[17,18]

Rietveld refined parameters such as unweighted profile R-factor (R_p), weighted profile R-factor (R_w), expected R-factor (R_e), goodness fit factor (χ^2) and lattice parameter (a_r) are given in Table 1. The values of χ^2 inform us about the good refining and quality of the samples.

The lattice parameter (a_{exp}) of Ni–Zn–Al–Nd ferrite nanoparticles was determined from X-ray data analysis using the relation:[19]

$$a_{exp} = \frac{\lambda\sqrt{h^2 + k^2 + l^2}}{2\sin\theta}$$

where λ is X-ray wave length, θ is the diffraction angle, and (h, k, and l) are Miller indices.

It is clear from the Table 1 that both lattices parameter (a_r and a_{exp}) and the unit cell volume increase with the Nd^{3+} contents. This increase is due to the change in ionic radius from Fe^{3+} (0.67 Å) to larger ionic radius of Nd^{3+} (0.99 Å).[20]

Furthermore, although Nd^{3+} ions have a larger ionic radius in comparison to that of Fe^{3+} ions, a very thin insulating ultra-thin layer may be formed around the grains due to ions that have spread over the grain boundary. This phenomenon can cause the contraction of the spinel lattice.[21]

Cation distribution plays a vital role in governing the structural, electrical and magnetic properties of AB_2O_4 spinel ferrites. Thus, the understanding of the cation distribution is essential in understanding the intricate structural and physical property relationship. Massoudi *et al.*[19] reported that the experimental intensities for the (220), (400) and (440) reflections are sensitive to cations on tetrahedral (A-) and octahedral (B-) site. In the present studies, the Bertaut method was adopted to compute the cation distribution estimated from XRD data.[22] From the best-matched intensity ratio, the cation distribution was estimated and the values are:

$$x = 0 \ (Zn_{0.4}Al_{0.28}Fe_{0.32}) \ [Ni_{0.6}Al_{0.22}Fe_{1.18}]$$

$$x = 0.05 \ (Zn_{0.4}Al_{0.28}Fe_{0.32}) \ [Ni_{0.6}Al_{0.22}Nd_{0.05}Fe_{1.13}]$$

$$x = 0.075 \ (Zn_{0.4}Al_{0.28}Fe_{0.32}) \ [Ni_{0.6}Al_{0.22}Nd_{0.075}Fe_{1.105}]$$

$$x = 0.1 \ (Zn_{0.4}Al_{0.28}Fe_{0.32}) \ [Ni_{0.6}Al_{0.22}Nd_{0.1}Fe_{1.08}]$$

For cubic spinel structures, the distance between magnetic ions (hopping length) in A site (tetrahedral) and B site (octahedral) (L_A and L_B) on A-site and B-site were calculated by using the following relations:[23]

$$L_A = \frac{a\sqrt{3}}{4}, \quad L_B = \frac{a\sqrt{2}}{4}$$

It is obvious from the Table 2 that the value of hopping length of A-site (L_A) is bigger than that of B site L_B, which leads to deduce that the electron hopping between ions at B and B sites is more probable than that between A and B sites.

The theoretical lattice parameter (a_{th}) can be calculated using the following equation:[19]

$$a_{th} = \frac{8\left[(r_A + R_O) + \sqrt{3}\,(r_B + R_O)\right]}{3\sqrt{3}}$$

where, R_O is the radius of the oxygen ion (1.32 Å), $r_A = \sum_i C_i r_i$ and $r_B = \frac{1}{2}\sum_i C_i r_i$ are the average ionic radii per molecule for the respective A and B-sites; here, C_i is the concentration of the element i with ionic radius r_i on a particular site.

The increase of hopping length and radius of the ion with an increasing substitution of Nd^{3+} ions is related to the increase in lattice constant and to the difference in the ionic radii of Nd^{3+} ions and Fe^{3+} ions, which means that the magnetic ions move far from other ions (Table 1).

The oxygen positional parameter (u) can be determined using the relations:

$$u = \left[(r_A + R_O)\frac{1}{a\sqrt{3}} + 0.25\right]$$

As shown in Table 2, (u) decreased from 0.3879 Å to 0.3874 Å with the Nd substitution. According to many researchers, u would be expected to be 0.375 Å for the origin at tetrahedral sites and a centric crystal structure.[24] According to XRD studies

Table 1 Summary of the structural parameters of $Ni_{0.6}Zn_{0.4}Al_{0.5}$-$Fe_{1.5-x}Nd_xO_4$ (x = 0.0, 0.05, 0.075 and 0.1) nanoparticle samples

Parameter	$x = 0.0$	$x = 0.05$	$x = 0.075$	$x = 0.1$
Space group	$Fd\bar{3}m$	$Fd\bar{3}m$	$Fd\bar{3}m$	$Fd\bar{3}m$
a_r (Å)	8.347	8.351	8.350	8.354
a_{exp} (Å)	8.325	8.331	8.335	8.339
a_{th} (Å)	8.354	8.375	8.387	8.543
V (Å^3)	577.1	582.4	582.3	583.1
χ^2	1.29	1.8	1.75	3.7
R_p (%)	24.9	23.1	18.6	35.5
R_{wp} (%)	11.1	11.9	10.6	17.1
R_e (%)	9.71	8.84	8.03	8.89
ρ_{X-ray} (g cm^{-3})	5.124	5.176	5.227	5.277
ρ_{th} (g cm^{-3})	3.334	3.314	3.234	3.321
P (%)	34.93	35.97	38.12	37.06
S (m^2 g^{-1})	39.56	37.88	39.17	39.34
D_{sc} (nm)	29.8	30.6	29.3	28.9
D_{wh} (nm)	62	70	65	59
$\varepsilon \times 10^{-3}$	1.96	2.9	3.1	1.9
D_{sem} (nm)	37.62	—	—	35

Table 2 Values of hopping lengths (L_A and L_B), ionic radii, the tetrahedral and octahedral bond lengths (d_{AE}) and (d_{BE}), tetrahedral edge (d_{AL}), shared and unshared octahedral edge (d_{BL}) and (d_{BEU}), interatomic bond lengths and angles for $Ni_{0.6}Zn_{0.4}Al_{0.5}Fe_{1.5-x}Nd_xO_4$ (x = 0.0, 0.05, 0.075 and 0.1) nanoparticle samples

Parameter	$x = 0.0$	$x = 0.05$	$x = 0.075$	$x = 0.1$
L_A (Å)	3.614	3.616	3.615	3.617
L_B (Å)	2.951	2.952	2.952	2.953
r_A (Å)	0.6492	0.6492	0.6492	0.6492
r_B (Å)	0.6429	0.6525	0.6568	0.7152
U (Å)	0.3875	0.3874	0.3873	0.3872
d_{AE} (Å)	3.247	3.237	3.236	3.236
d_{BE} (Å)	2.639	2.653	2.656	2.660
d_{AL} (Å)	1.998	1.982	1.982	1.981
d_{BL} (Å)	1.979	1.984	1.986	1.988
d_{BEU} (Å)	2.951	2.952	2.953	2.955
p (Å)	1.973	1.979	1.981	1.983
q (Å)	1.988	1.982	1.982	1.981
r (Å)	3.807	3.796	3.795	3.794
s (Å)	3.666	3.667	3.668	3.669
b (Å)	2.943	2.945	2.946	2.948
c (Å)	3.451	3.453	3.455	3457
d (Å)	3.604	3.607	3.609	3.610
e (Å)	5.407	5.411	5.413	5.416
f (Å)	5.098	5.101	5.104	5.106
θ_1 (°)	121.16	121.32	121.34	121.40
θ_2 (°)	136.18	136.71	136.85	137.00
θ_3 (°)	127.72	127.39	127.28	127.23
θ_4 (°)	126.68	126.61	126.63	126.60
θ_5 (°)	68.87	69.26	69.34	69.40

of some researchers, $u > 0.375$ Å for substituted ferrites.[19,25] In the present study, u was determined to be higher than its expected "ideal" value of 0.375 Å.

The tetrahedral and octahedral bond lengths (d_{AE}) and (d_{BE}), tetrahedral edge (d_{AL}), shared and unshared octahedral edge (d_{BL}) and (d_{BEU}) can be evaluated by:[26]

$$d_{AE} = a\sqrt{2}\left(2u - \frac{1}{2}\right)$$

$$d_{AL} = a\sqrt{3}\left(u - \frac{1}{4}\right)$$

$$d_{BL} = a\sqrt{3(u)^2 - \frac{11}{4}u + \frac{43}{64}}$$

$$d_{BEU} = a\sqrt{4(u)^2 - 3u + \frac{11}{16}}$$

$$d_{BE} = a\sqrt{2}(1 - 2u)$$

As shown in Table 2, d_{AE}, d_{AL} decrease while d_{BE}, d_{BEU} and d_{BL} increase with an increase in Nd^{3+} content. These variations can be explained by the fact that as Nd^{3+} ions preferred to occupy the octahedral B sites where they have replaced the Fe^{3+} ions. Since the radius of Fe^{3+} ion is smaller than the radius of Nd^{3+} ions hence the increasing trend is then justified.

The bond lengths and bond angles between the cations are calculated by the following relations:[19]

Me–O distances

$$p = a\left(\frac{5}{8} - u\right), \quad q = a\sqrt{3}(u - 0.25), \quad r = a\sqrt{11}(u - 0.25), \quad s = a\sqrt{3}\left(\frac{1}{3}u + \frac{1}{8}\right),$$

Me–Me distances

$$b = \frac{a\sqrt{2}}{4}, \quad c = \frac{a\sqrt{11}}{8}, \quad d = \frac{a\sqrt{3}}{4}, \quad e = \frac{3a\sqrt{3}}{8}, \quad f = \frac{a\sqrt{6}}{4},$$

Bond angles

$$\cos(\theta 1) = \frac{p^2 + q^2 - c^2}{2pq}, \quad \cos(\theta 2) = \frac{p^2 + r^2 - e^2}{2pr},$$

$$\cos(\theta 3) = \frac{p^2 - b^2}{2p^2}, \cos(\theta 4) = \frac{p^2 + s^2 - f^2}{2ps}\cos(\theta 5)$$

$$= \frac{r^2 + q^2 - d^2}{2rq},$$

where (a) is the experimental lattice parameter. All the calculated bond angles and bond lengths are listed in Table 2, where all bond angles changed irregularly in the system. Therefore,

the weakening and strengthening of the magnetic interactions between different cations were affected by the concentration of Nd^{3+} doping in the system.

The X-ray density ($\rho_{X\text{-ray}}$) of the samples was calculated by considering that a basic unit cell of the cubic spinel structure contained eight ions using the following equation:[27,28]

$$\rho_{X\text{-ray}} = \frac{8M}{N_A a^3}$$

where "M" is the molar weight of each compound, "N_A" is Avogadro's number; "a" is the as-calculated lattice parameter converted in cm units and 8 represents the number of molecules in a unit cell of spinel lattice.

The bulk density ρ_{th} was estimated using the following relation:[29]

$$\rho_{th} = \frac{m}{\pi r^2 h}$$

where m, r and h are respectively the mass, the radius and the thickness of the pellet.

The apparent porosity, P, for each sample was calculated using the following equation:[29]

$$P(\%) = \frac{\rho_{X\text{-ray}} - \rho_{th}}{\rho_{X\text{-ray}}} \times 100$$

The change in X-ray density and bulk density leads to an increase in porosity after adding the neodymium which is possibly originated from the vacancies created from the change of ionic radii.[20]

The average crystallite size of our samples was calculated from the full width at the half maximum (FWHM) of the most intense peak by using the Debye–Scherrer equation:[30]

$$D_{SC} = \frac{0.9\lambda}{\beta \cos \theta}$$

where λ is the wave length of the used X-ray radiation, θ is Bragg's angle of the most intense peak and β is its angular full width at half maximum of peak at FWHM for the most intense peak. The calculated values of average crystallite size D_{SC} are listed in Table 1. As noticed, the average crystallites size is found to be decreasing approximately when increasing the doping level x. This decrease can be explained based on the ionic radii of substituent. Moreover, this may also have been due to the reaction condition that favored the formation of nano ferrite, which prevented the growth of more particles. These crystal size values are small sufficient to achieve the signal-to-noise ratio in high-density recording media and medical applications.

The Williamson–Hall (W–H) equation was also used to determine the average crystallite size and lattice strain in all the samples and can be expressed as followed:[31]

$$\beta \cos \theta = \frac{K\lambda}{D_{WH}} + 4\varepsilon \sin \theta$$

where, β is the full width at half maximum of the XRD peaks, θ is the position of the peaks, K is the Debye–Scherrer constant (0.94 for spherical shaped nanoparticles), λ is the X-ray wave length, D_{wh} is the size of the crystallite and ε is the average micro strain.
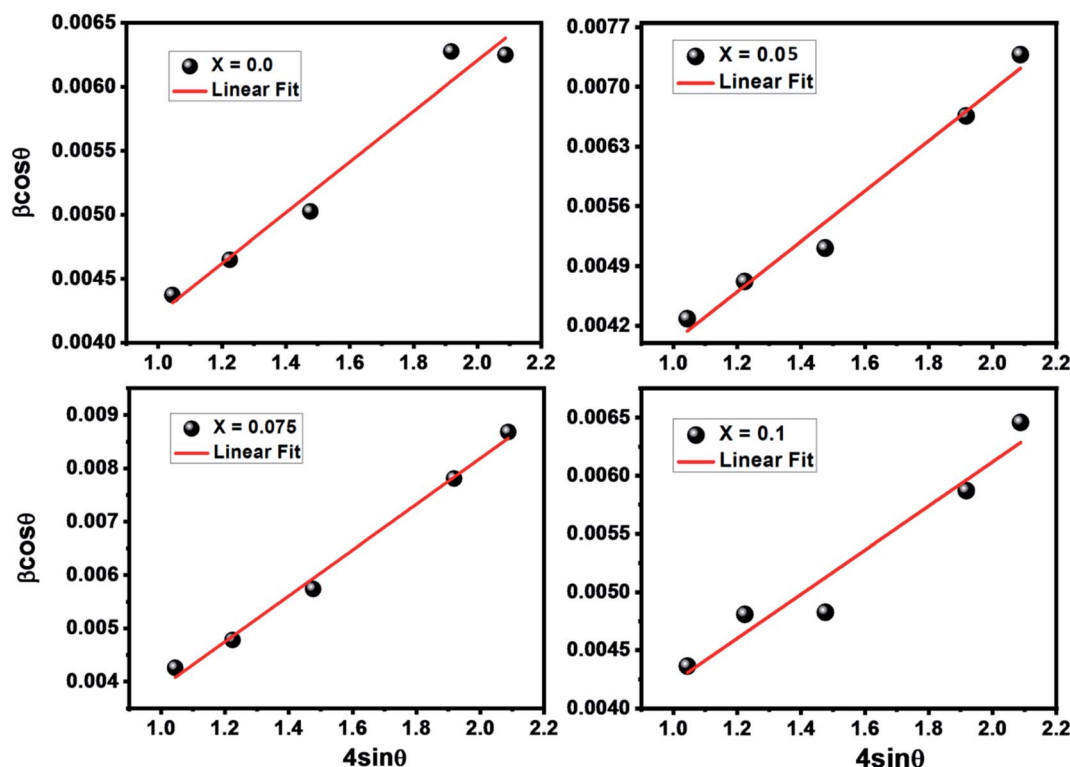
Fig. 2 W–H plots for Nd^{3+} substituted Ni–Zn–Al ferrite samples.

A linear plot of $\beta \cos \theta$ *versus* $4 \sin \theta$ yields intercept as crystallite size and the slope as strain as shown in Fig. 2. The results are tabulated in Table 1. The observed positive slope in W–H plot confirmed the tensile strain experienced in smaller grain size.[32] Moreover, the obtained values of lattice strain ε are in the range of 1.9×10^{-3} to 3.1×10^{-3} (Table 2). These values of lattice distortion are comparable with those previously reported for ferrite spinel.[33,34]

Assuming all the particles to be spherical, the specific surface area was calculated from the relation:[35]

$$S = \frac{6000}{D\rho_{\text{X-ray}}}$$

where D is the diameter of the particle, "$\rho_{\text{X-ray}}$" is the X-ray density and the constant 6000 is called form factor for spherical particles. The specific surface area values are listed in Table 1. These values of specific surface area were relatively high, indicating that our samples nanoparticles are potential candidates for gas sensing applications.[36]

Besides, the external morphology of $Ni_{0.6}Zn_{0.4}Al_{0.5}Fe_{1.5-x}Nd_xO_4$ ($x = 0.00$ and 0.1) was visualized by SEM. The micrograph of the samples (indicated in Fig. 3a and b) shows clear indistinguishable grain boundaries and high surface energy. Both samples showed susceptibility towards clusters thanks to reciprocal magnetic interactions and electrostatic effects emerging among of ferrites. Having a closer look at the images, it can be observed that not regular spherical shaped and nanosize of the grains. These results are analogous to other researcher's work made previously such as P. P. Naik *et al.* who

reported in their publication[12] that "large agglomerates of many particles are formed". Furthermore, the surface morphology exposes distribution of small grains at the grain boundaries, which is the unique mark of Ni–Zn ferrites. The obtained grain size results from SEM micrographs for $x = 0.00$ and $x = 0.1$ as shown in Fig. 3c and d (using the Image J software by fitting the particle size distribution with a Lorentz function) are 37.62 and 35 nm for $x = 0.00$ and $x = 0.1$, respectively. This reduction in grain size was also discovered by P. P. Naik *et al.*[12] who have found that neodymium prefers to occupy octahedral sites which leads to strain on the grain boundaries causing an obstacle in grain growth and consequently the downturn of grain distribution with augmenting the Nd^{3+} doping level. By comparing the average size of the crystallites obtained from XRD and the particle size of the SEM analysis, we can deduce that every grain is almost monocrystalline, which confirms the nanometric size of our samples. It is well known that dispersive X-ray analysis (EDX) is a useful technique for chemical analysis and for estimating the atomic percentages of different constituents on surface layer of the solid investigated. Energy dispersive X-ray analysis was performed for prepared samples $x = 0.00$ and $x = 0.1$ and presented in Fig. 3e and f. The EDX spectrum confirm the presence of Fe, Ni, Zn, Al, Nd and O elements in the samples without any traceable impurities and confirms further the phase pure of Ni–Zn ferrite samples.

FTIR measurements

The Fourier-Transform Infrared (FTIR) spectra of $Ni_{0.6}Zn_{0.4}Al_{0.5}Fe_{1.5-x}Nd_xO_4$ samples with $x = 0.00$; 0.05; 0.075 and 0.1 are
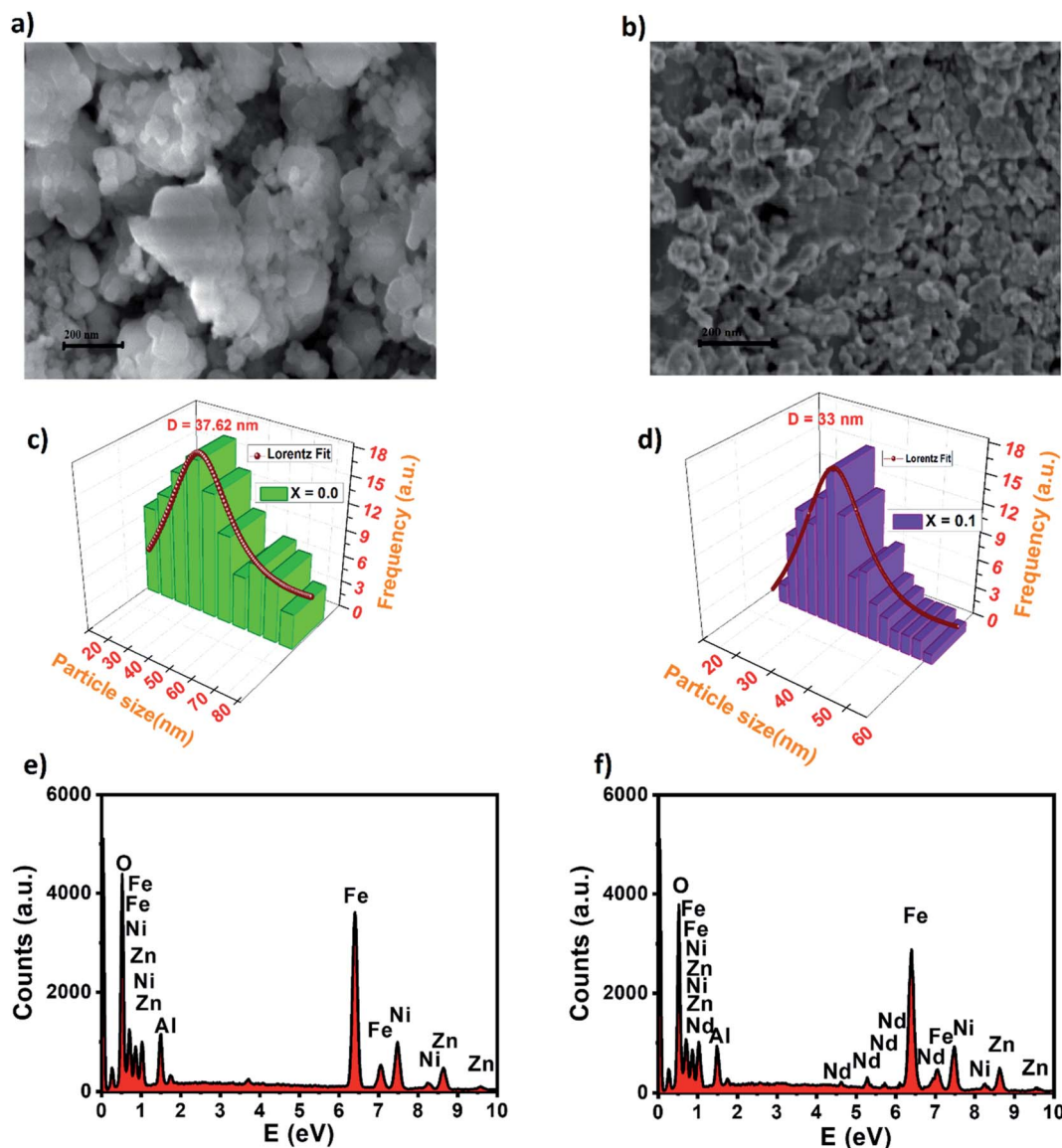
Paper

Fig. 3 SEM micrograph of nickel–zinc ferrites for (a) $x = 0.00$, (b) $x = 0.1$, particle size distribution for (c) $x = 0.00$ and (d) $x = 0.1$ and EDX spectrum of (e) $x = 0.00$ and (f) $x = 0.1$.

studied in the range of 400–4000 cm^{-1} as illustrated in Fig. 4. As known for spinel ferrites, it exist two major metal–oxygen frequency bands v_1 and v_2 corresponding respectively to the metal ions stretching vibration in the tetrahedral site and that in the octahedral site.[37–39] In our case, the higher frequency absorption band v_1 is assigned for Fe^{3+}–O intrinsic vibration of tetrahedral group in the range of 570 cm^{-1} and the lower frequency absorption band v_2 is attributed to that of the octahedral group near 405 cm^{-1} which is the fingerprint of Zn–Ni ferrites.[39,40] There are additional frequency band located near 1061 cm^{-1} corresponding to the O–H stretching vibrations.[41]

It can be noted from the figure that the peaks intensity amplifies with raising the Nd^{3+} doping level. Such behavior can be justified by the changes in bond lengths of Fe^{3+}–O tetrahedral and octahedral sites due to the insertion of doping ion Nd^{3+}.[37] Moreover, the vibration band (v_1) is widened and shifted towards the higher wavenumber region with an increased Nd^{3+} doping level (see Table 3). Same behavior was observed in Nd doped $Mn_{0.6}Zn_{0.4}Fe_2O_4$ reported by Naik *et al.*[12] This shifting is

Table 3 Absorption bands (v_1 and v_2), force constant (K_T and K_O for the A and the B sites, respectively) and the Debye temperature of $Ni_{0.6}$-$Zn_{0.4}Al_{0.5}Fe_{1.5-x}Nd_xO_4$ ($x = 0.0$, 0.05, 0.075 and 0.1) nanoparticle samples

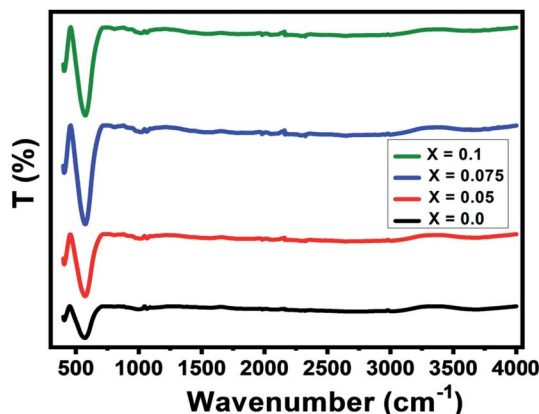| Parameter	$x = 0.0$	$x = 0.05$	$x = 0.075$	$x = 0.1$
v_1 (cm^{-1})	571	572	573	576
v_2 (cm^{-1})	407	406	409	410
v_a (cm^{-1})	489	489	491	493
K_T (N m^{-1})	133.2	130.0	128.4	124.6
K_O (N m^{-1})	177.1	184.4	188.7	192.8
θ_D (K)	703	703	706	708

Fig. 4 FTIR transmittance spectra of Nd^{3+} doped Ni–Zn ferrites.

also associated with the lattice constant variations. However, the presence of these absorption bands further confirms the formation of our spinel-structured Ni–Zn–Al ferrite.

The force constants (K) for the tetrahedral site (K_T) and octahedral site (K_O) can be calculated using the following relation:[35]

$$K_{T,O} = 4\pi C^2 \nu_{1,2}{}^2 \mu$$

where, C is the velocity of light ($C = 2.99 \times 10^8$ m s^{-1}), $\nu_{1,2}$ is the vibration frequency for tetrahedral or octahedral sites in m^{-1} and μ is the reduced mass for the Fe^{3+} ions and the O^{2-} ions ($\sim 2.065 \times 10^{-26}$ kg mol^{-1}).

The calculated values of the force constants (K_T) and (K_O) are listed in Table 3. The force constants of the A and B sites increase with increasing the doping level x. This increase may

be due to the motion of metallic ions between the A- and B-site, which changes the site radius, and variation in bond lengths, d_{A-O} and d_{B-O}.

The Debye temperature (θ_D) can be calculated using the equation given by Waldron:[35]

$$\theta_D = \hbar C \nu_a / k_B = 1.438 \nu_a$$

where, $\hbar = h/2\pi$, h is Planck's constant, ν_a is the average value of wavenumbers, k_B is Boltzmann's constant and C is the velocity of light. For ferrites, we get $\hbar C/K_B = 1.438$. After calculating, we discovered that θ_D increase within creasing Nd^{3+} doping level (Table 3). When we refer to the specific heat theory,[42] we found that this increase of Debye temperature may refer to a decrease of the conduction electron number Ne (n-type) and to an increase of the number of conduction holes Np (p-type).

Raman spectroscopy

To shed more light on the vibrational study and confirm the formation of our compounds, we perform Raman scattering analysis at room temperature. Raman spectra in the region of 100 cm^{-1} to 850 cm^{-1} by using 540 nm laser excitation for $Ni_{0.6}Zn_{0.4}Al_{0.5}Fe_{1.5-x}Nd_xO_4$ samples are presented in Fig. 5. It is well known that the spinel ferrite belong to $Fd\bar{3}m$ space group which gives rise to 39 normal vibrational modes, five of them are Raman active modes ($A_{1g} + E_g + 3T_{2g}$).[43] In spinel ferrites, it exist two modes: the first is vibrations of the oxygen atoms in tetrahedral sites AO_4 groups above 600 cm^{-1}, and the second mode below this frequency is vibrations of the oxygen atoms in octahedral sublattice. The translation movement of the entire tetrahedral units MO_4 is associated to $T_{2g}(1)$ phonon. The $T_{2g}(2)$ and $T_{2g}(3)$ Raman modes refer respectively to the symmetric and asymmetric bending of the oxygen atom in the metal–
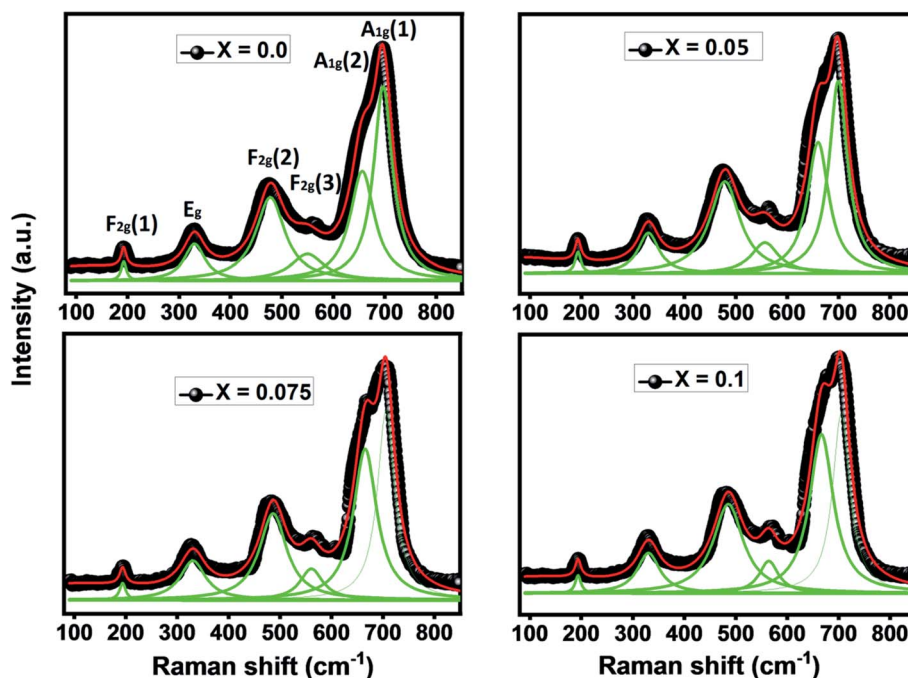

Fig. 5 Raman spectra of the $Ni_{0.6}Zn_{0.4}Al_{0.5}Fe_{1.5-x}Nd_xO_4$ for different values of Nd^{3+} concentration.

© 2021 The Author(s). Published by the Royal Society of Chemistry

Table 4 Raman band position of $Ni_{0.6}Zn_{0.4}Al_{0.5}Fe_{1.5-x}Nd_xO_4$ ($x = 0.0$, 0.05, 0.075 and 0.1) nanoparticle samples

| Raman band position (cm^{-1})	$x = 0.0$	$x = 0.05$	$x = 0.075$	$x = 0.1$
$A_{1g}(1)$	691.5	697.2	701.3	702.4
$A_{1g}(2)$	651.3	665	670.2	671.5
$F_{2g}(3)$	493.5	497.9	559.1	563.4
$F_{2g}(2)$	468.3	482.9	484.8	485.7
E_g	330.8	330.9	331.7	332.9
$F_{2g}(1)$	191.3	193.1	193.3	193.6

oxygen band at the octahedral site. Plus, the E_g Raman mode is correlated to the symmetric bending of the oxygen atom with respect to the metal ion at the octahedral site. Finally, the symmetric stretching of the oxygen atom in tetrahedral sites corresponds to A_{1g} Raman mode.[44] In order to better analyze the Raman results of our samples, Lorentzian function was used to fit the obtained Raman data. The Raman modes for all $Ni_{0.6}$-$Zn_{0.4}Al_{0.5}Fe_{1.5-x}Nd_xO_4$ samples ($x = 0.00$, $x = 0.05$ $x = 0.075$ and $x = 0.1$) are summarized in Table 4. These Raman band positions are in accord with previous researches about spinel ferrite.[32,45] It is clear from the Table 4 that all modes of $Ni_{0.6}$-$Zn_{0.4}Al_{0.5}Fe_{1.5-x}Nd_xO_4$ are shifting to high frequency with increasing Nd^{3+} content. This shift in Raman modes is due to cation redistribution between octahedral and tetrahedral sites result from the incorporation of Nd^{3+} ions in spinel ferrite samples. Furthermore, the broad and shift of the Raman modes in the nano-particle can be also ascribed to phonon confinement and variations inphonon relaxation with the smaller particle size.[35] From Fig. 5, we observe that no additional peak matching any other iron oxide phase is found for the compounds (monophasic composition), which confirms the results already found by the XRD analysis. In contrast with XRD analyze, it reveals that the absence of the orthoferrite phase $NdFeO_3$ for $x = 0.1$ sample, which may be due to low percentage of this phase in the system. However, we conclude that all the Raman active bands of our samples are conforming to the

theoretical vibrational modes of the spinel ferrites with cubic phase $Fd\bar{3}m$ space group, which also confirms the formation of Nd doped Ni–Zn–Al ferrite samples.

Magnetic study

The temperature *versus* magnetization curves for all studied samples were measured over a temperature range of 300–750 K under an external magnetic field of 1 kOe, as shown in Fig. 6. As clear in the figure, magnetization decreased continuously with temperature increasing till reaching a minimum value. This is probably caused by the thermal randomization of magnetic moments at various lattice sites.[46] The T_C values corresponding to the point of inflection in $M(T)$ curves were determined from the first derivative of these curves (inset of Fig. 6). T_C values are found to be decreasing approximately with increasing the Nd doping level x from 623 K for $x = 0.00$ to 591 K for $x = 0.1$ (see Table 5). This decrease in the value of Curie temperature with increasing Nd content may be due to a change in cation distribution between the tetrahedral and octahedral sites of the spinel lattice on the basis of strength of the exchange interactions. S. G. Kakade *et al.*[45] reported that the Curie temperature decreases with Er substitution in $CoFe_2O_4$ due to decreasing the strength of A–B sublattice superexchange interactions. For the spinel oxides AB_2O_4, as reported by Néel about the two-sublattice model of ferrimagnetism,[47] the magnetic properties are governed by competition among the magnetic interactions between ions occupying the A and B sub-lattices: the intrasite J_{AA} and J_{BB}(A–O–A and B–O–B) and the strongest and most dominant A–B sub-lattice exchange J_{AB}. So, the replacement of iron by neodymium causes a weakening of the interaction J_{AB} triggered by the presence of non-magnetic Nd^{3+} ions the crystallographic sites of the Ni–Zn–Al ferrite, and as a result of this, the Curie temperature decreases.[48] As shown in Tables 1 and 2, the increase in lattice parameter, bond angles and bond lengths results in decreased A–B exchange interaction. As the exchange interaction is relatively strong, correspondingly higher thermal energy is required to disorient the moments,[19] thereby resulting in lower T_C values with increasing the Nd doping level x.

Fig. 7 depicts the inverse of susceptibilities *versus* temperature which ascend clearly when the ferrite nanoparticles change
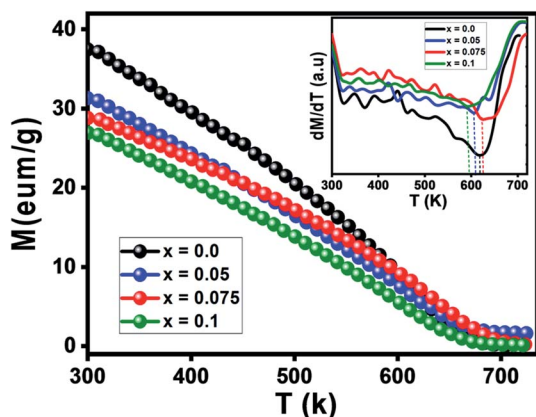
Fig. 6 $M-T$ variation curves of Ni–Zn nanoferrites. Inset: variation of dM/dT *versus* temperature.

Table 5 Summary of the magnetic parameters of $Ni_{0.6}Zn_{0.4}Al_{0.5}$-$Fe_{1.5-x}Nd_xO_4$ ($x = 0.0$, 0.05, 0.075 and 0.1) nanoparticle samples

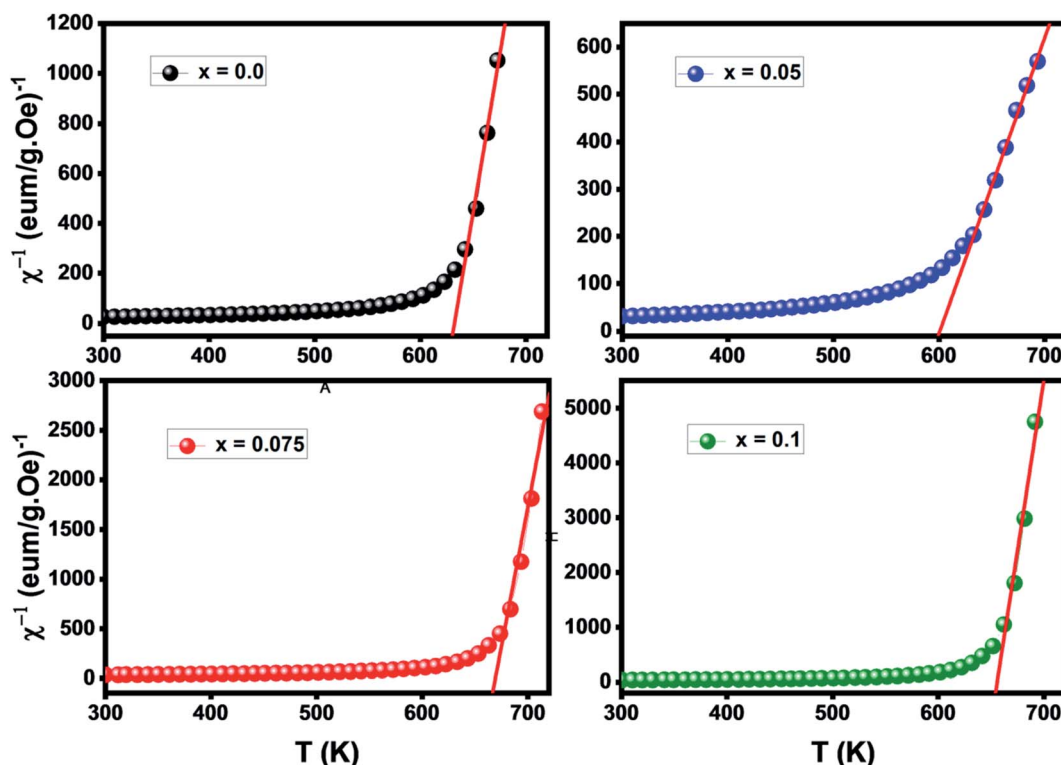| Parameter	$x = 0.0$	$x = 0.05$	$x = 0.075$	$x = 0.1$
T_C (K)	623	622	606	591
θ_{CW} (K)	668	601	669	655
μ_{eff} (μ_B)	3.13	1.13	0.37	0.25
M_s (emu g^{-1})	47	42	39.8	34
H_c (Oe)	34	25	20	15
M_r (emu g^{-1})	3.2	2	1.5	0.5
M_r/M_s	0.07	0.08	0.04	0.01
K_1 (J m^{-3})	5.9×10^4	5×10^4	3.9×10^4	4.2×10^4
n_B (μ_B)	1.87	1.7	1.63	1.41
n_{th} (μ_B)	5.5	5.4	5.35	5.3
Y–K angles (°)	60.74	61.87	62.3	69.26

Fig. 7 Inverse of susceptibility *versus* temperature of Ni–Z spinel ferrites.

its magnetic state from ferrimagnetic to paramagnetic. In the temperature range, well above T_C, the susceptibility follows the Curie–Weiss law:[49]

$$\chi^{-1}(T) = \frac{T - \theta_{CW}}{C}$$

where θ_{CW} is the Curie–Weiss paramagnetic temperature, T is the absolute temperature and C is the Curie constant. The experimental effective moment μ_{eff} (in unit of Bohr magneton μ_B) has been calculated, using C values gotten from the slope of $1/\chi$ and has been expressed as:

$$\mu_{eff}^{exp} = \sqrt{\frac{3 \times k_B \times C}{N_A}} = \sqrt{8C}\mu_B$$

where N_A is Avogadro number, k_B is Boltzmann constant and μ_B is Bohr magneton. The obtained parameters θ_{CW} and μ_{eff} are listed in Table 5. As noticed from the table, the obtained values of θ_{CW} are slightly great comparable to T_C. This difference may mostly caused by the presence of a magnetic inhomogeneity.[50]

Generally, the difference between T_C and θ_{CW} is associated with the presence of short-range ordered slightly above T_C. However, we mark a downturn in Curie temperature and θ_{CW}
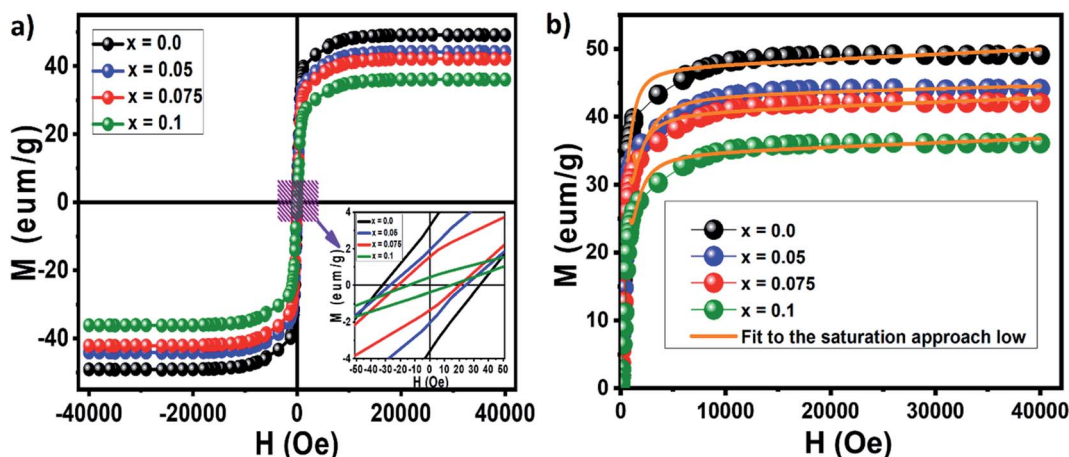

Fig. 8 Magnetic hysteresis loops obtained for the nanocrystalline undoped and neodymium-doped Ni–Zn–Al ferrite ($Ni_{0.6}Zn_{0.4}Al_{0.5}Fe_{1.5-x}$-$Nd_xO_4$) powders (a) and *M*–*H* variation curves (b).

values which can be related to the weakening of A–B exchange interactions caused by the replacement of iron (Fe^{3+}) by the neodymium (Nd^{3+}). The decrease in the effective experimental paramagnetic moment with the increase in Nd^{3+} content may refer to the decrease in ferrimagnetic clusters present in the paramagnetic phase.[51]

The magnetic hysteresis loops obtained for the nano-crystalline undoped and neodymium-doped Ni–Zn–Al ferrite ($Ni_{0.6}Zn_{0.4}Al_{0.5}Fe_{1.5-x}Nd_xO_4$) Powdersat room temperature are shown in Fig. 8a. All the compositions exhibit typical soft ferrimagnetic nature. It could be observed from the hysteresis loop that all composition of nanoparticles shows negligible remanence and coercivity, which confirms the presence of super paramagnetic behavior in the samples. Moreover, the hysteresis loops are not well-saturated which may be related either to super paramagnetic state or to spin disorder at the surface of thin nanoparticles.[19,52,53]

However, all samples exhibits a super paramagnetic behavior might be useful for biomedical applications such as hypothermia and contrast enhancement agents for magnetic resonance imaging (MRI).

Magnetic parameters such as saturation magnetization (M_s), coercivity (H_c), remanent magnetization (M_r), magneto-crystalline anisotropy constant (K_1) and reduced magnetization (M_r/M_s) were obtained from the hysteresis loop. The saturation magnetization (M_s) and magneto-crystalline anisotropy constant (K_1) were obtained from the hysteresis loop by fitting the high field magnetization data (Fig. 8b) using the saturation approach low:

$$M = M_S\left(1 - \frac{A}{H} - \frac{B}{H^2}\right) + C \times HB = \frac{8}{10^5}\frac{K_1^2}{M_S^2}$$

where M_S is the saturation magnetization, H is the applied external magnetic field, A and B are a constant, C symbolize the susceptibility in the high field region and K_1 is the first order cubic magneto-crystalline anisotropy coefficient in J m^{-3}. The different magnetic parameters are tabulated in Table 5. It is observed from hysteresis loop that the saturation magnetization decreases from 47 emu g^{-1} (for $x = 0.00$) to 34 emu g^{-1} (for $x = 0.1$) with increasing the Nd^{3+} doping level in Ni–Zn–Al ferrite. The decrease of saturation magnetization may refer to the passage of Fe^{3+} from octahedral to tetrahedral sites with Nd^{3+} ions substitution in Ni–Zn–Al ferrite. As evidenced from Table 2, the distance between cation and anion decreases while the distance between cations increases with an increasing substitution of Nd^{3+} ions. It is noted that θ_1 and θ_2 related to the A–B interaction increase, θ_3 and θ_4 related to the B–B interaction decrease, whereas θ_5 corresponding to the A–A interaction slightly increases with the Nd^{3+} substitution. It is reported by Wang et al.[25] that the increase in inter-ionic distances between cation–cation results in weakening of the strength of magnetic interactions. In fact, in the present work, we have observed the increase in inter-ionic distances between cation–cation, suggesting weakening of the A–B super-exchange interactions but contrary to this, we also observed an increase in θ_1, θ_2 and θ_5 which suggests the strengthening of the A–B and A–A interactions and decrease in θ_3 as well as θ_4 indicates the weakening of the B–B interaction, indicating the magnetism observed within the cation distribution framework could not be demonstrated. A similar observation results has been reported of Nd doped Mg–Mn spinel ferrite nanoparticles.[54] Since the inter-ionic distance and bond angles are suggesting conflicting information, the decrease in saturation magnetization is attributed to the surface effect of the magnetic nanoparticles, due to small crystallite size.[19] This surface effect can be elucidated by postulating the existence of dead magnetic layer due to the surface spin disorder. It is expected that the number of spins at the surface of Nd^{3+} doped Ni–Zn–Al ferrite increases as the crystallite size get smaller.[55] It is further noticed from the XRD analysis that for higher substitution of Nd^{3+} ions, small traces of secondary phase $NdFeO_3$ is noticed. The $NdFeO_3$ is antiferromagnetic in nature, a decrease in saturation magnetization expected for higher concentrations of Nd.[56] Thus, the resultant of the above mentioned effects are expected to reflect in the saturation magnetization of pure and Nd doped Ni–Zn–Al ferrite nanoparticles.

Moreover, the decrease in saturation magnetization of our ferrite samples can be explained on the basis of magnetic moment of metal ions in the samples. Magnetic moment of Nd^{3+} ion (3 μ_B)[57] is smaller than that of Fe^{3+} ion (5 μ_B),[58] when Fe^{3+} ions in nanoparticles spinel $Ni_{0.6}Zn_{0.4}Al_{0.5}Fe_{1.5}O_4$ are partially doped by Nd^{3+} ions, the Nd^{3+} ions are preferentially occupied the octahedral sites (B-sites), which leads to the decrease in the net magnetic moment of octahedral sites in $Ni_{0.6}Zn_{0.4}Al_{0.5}Fe_{1.5-x}Nd_xO_4$ with the rise of x. Similar saturation magnetization behavior has been reported for many rare earth doped spinel ferrites.[59–62]

The effective anisotropy constants K_1 of $Ni_{0.6}Zn_{0.4}Al_{0.5}Fe_{1.5-x}Nd_xO_4$ are showed in Table 5. K_1 value decreases with the increase in Nd content.

The change in the magnetic parameters is due to the influence of cationic stoichiometry and occupancy at specific sites. In the present study, based on the cation distribution obtained from DRX, a deviation in the regular preferences of cations was observed. Ni^{2+} ions mainly occupy the octahedral sites whereas Zn^{2+} has strong preference for the tetrahedral sites, Al^{3+} and Fe^{3+} ions have a preference for both the available A and B sites and the Nd^{3+} ions are preferentially occupied the B sites. The corresponding magnetic moments of Ni^{2+}, Nd^{3+}, Zn^{2+}, Al^{3+} and Fe^{3+} are 2 μ_B, 3 μ_B, 0 μ_B, 0 μ_B and 5 μ_B, respectively. By applying the collinear Néel two-sub-lattice model on the different assumed cation distribution configurations, the calculated magnetic moment value can be determined using the following formula:

$$n_{th} = M_B - M_A$$

where M_A and M_B are the sub-lattice magnetization, which can be calculated from the magnetic moment of each cation in terms of Bohr magneton (μ_B).

The dependence of the observed magnetic moment per formula unitin Bohr magneton (μ_B) with Nd^{3+} substitution in Ni–Zn–Al ferrite, is summarized in Table 5 after being calculated using the relation below:[19]

$$n_B = \frac{M \times M_S}{5585}$$

where M is the molecular weight of a particular ferrite composition and M_S is saturation magnetization (emu g^{-1}). The decrease in magnetic moment n_B from 1.87 μ_B (at $x = 0.00$) to 1.41 μ_B (at $x = 0.1$) with elevating the Nd^{3+} concentration in Ni–Zn–Al ferrite is also noticed. The variation trends of net magnetic moment (n_{th}) and observed magnetic moment (n_B) are similar while the values of observed magnetic moment (n_B) are lower than that of net magnetic moment (n_{th}). It indicates that the magnetization behavior for all samples cannot be explained on the basis of Néel two-sublattice model, suggesting the dominant role of canted spin (non-collinear) on B sites and the existence of Yafet–Kittel angle. Spin orientations of magnetic ions line up with making angles from the favorite direction. This behavior is called spin canting or non-collinear magnetic order. The Yafet–Kittel angles (a_{Y-K}) are calculated from the observed magnetic moment n_B values according to the relation below:[63]

$$n_B = M_B \quad \cos \quad \alpha_{Y-K} - M_A$$

The obtained values of Y–K angles are summerized in Table 5. It increases when Nd^{3+} concentration elevates, indicating increased contribution of non-collinear nature for magnetization variation. The non-zero Y–K angles support that the magnetization behavior can't be represented on the basic of Néel two sub-lattice model due to the presence of spin canting on the octahedral site (B site), which rises the B–B interaction, as a result the A–B interaction reduces.

Table 5 also shows that the coercivity (H_c) decreases from 35 Oe to 15 Oe as x is increased from $x = 0.00$ to $x = 0.1$. The decrease in coercivity is being attributed to the strong spin–orbit coupling of rare earth Nd^{3+} ions contribute to the anisotropy, when they are located in the B sites of ferrite. Another possible explanation is that the decrease in the size of the particles could cause a decrease in the coercivity. It is also found that the squareness ratio (M_r/M_s) decreases with increase Nd^{3+} substitution. The values of M_r/M_s for Nd-doped Ni–Zn–Al ferrites which vary from 0.08 to 0.01 are shown in Table 5. These values are less than the typical value of "0.5" expected for a single magnetic domain material.[53] The low value of M_r/M_s could be attributed to the interactions between the grains which, in turn, area affected by the grain size distribution in the material.

To probe if our samples can be useful for high-frequency microwave applications, it is essential to have available materials with a high microwave frequency value.[19,64] The microwave frequency (ω_m) was calculated by the given equation:

$$\omega_m = \gamma 8\pi^2 M_s$$

where M_s is the saturation magnetization and γ is the gyromagnetic ratio ($\gamma = 2.8$ MHz Oe). The calculated values of microwave frequency are 10.6, 9.3, 8.8, and 7.5 GHz for $x = 0.00$, $x = 0.05$, $x = 0.075$, and $x = 0.1$, respectively. Actually, the

obtained microwave frequency values for our samples are comparable and even much bigger than some systems used for high-frequency microwave applications noting Pr doped Cu nanoferrites (from 5.2–9.5 GHz)[64] and Al doped spinel nanoferrites (6–7 GHz).[65] Thus, we can affirm that the studied samples can be good candidates for high-frequency microwave applications.

In general, a large magnetocaloric effect (ECM) value is observed near the transition temperature and is closely related to the order of the corresponding magnetic phase transition. The $M(T)$ curves show a reversible character of the magnetization around the Curie temperature. Furthermore, the small area of the hysteresis cycle indicates low energy loss during a magnetization–demagnetization process. Therefore, the Nd doped Ni–Zn–Al ferrite can be considered as a candidate for magnetic refrigeration in a wide temperature range above room temperature and other various applications such as in biomedicine and in microwave devices.

Conclusion

The present study demonstrates the effect of Nd^{3+} substitution for Fe^{3+} in Ni–Zn ferrite nano-crystals morphology, structure and magnetic properties. Structural analysis of undoped and Nd^{3+} doped $Ni_{0.6}Zn_{0.4}Al_{0.5}Fe_{1.5-x}Nd_xO_4$ with $x = 0.00$, 0.05, 0.075 and 0.1 showed a spinel cubic structure with $Fd\bar{3}m$ space group. Because of the large ionic radius of neodymium, the lattice parameter, cell volume and crystallite size were found to be increasing when the doping level is rising. Spectroscopic analysis demonstrates the change in the frequency intensities which affects the bond length in Fe^{3+}–O tetrahedral and octahedral sites due to the insertion of doping ion Nd^{3+}. Magnetic study proves a ferrimagnetic–paramagnetic transition at the Curie temperature. The cationic arrangement between the tetrahedral (A-) and octahedral (B-) of Ni–Zn–Al ferrite samples was estimated from the diffraction intensities of XRD data. Based on the cation arrangement, the estimated magnetic moment values, by adopting Néel's sublattice and Yafet–Kittel models, M_s variation with x is explained and found to reduce with the rise in Nd content. The magnetic hysteresis loops showed a soft ferrimagnetic nature and the presence of super paramagnetic behavior in this material, which can be considered as a good criterion for biomedical applications. Furthermore, high values of microwave frequency (ω_m) in the range 7.5–10.6 GHz are also reported.

Conflicts of interest

There are no conflicts to declare.

Acknowledgements

References

1 Y. K. Dasan, B. H. Guan, M. H. Zahari and L. K. Chuan, Influence of La^{3+} Substitution on Structure, Morphology and Magnetic Properties of Nanocrystalline Ni–Zn Ferrite, *PLoS One*, 2017, **12**(1), e0170075.

2 L.-Z. Li, X.-X. Zhong, R. W. Wang, X.-Q. Tu, L. He and F.-H. Wang, *J. Magn. Magn. Mater.*, 2019, **475**, 1–4.

3 L. Andjelković, M. Šuljagić, M. Lakić, D. Jeremić, P. Vulić and A. S. Nikolić, A Study of the Structural and Morphological Properties of Ni–Ferrite, Zn–Ferrite and Ni–Zn–Ferrites Functionalized with Starch, *Ceram. Int.*, 2018, **44**(12), 14163–14168.

4 M. Abbas, B. P. Rao and C. G. Kim, *Mater. Chem. Phys.*, 2014, 1–9.

5 S. Kumar, P. Kumar, V. Singh, U. K. Mandal and R. K. Kotnala, *J. Magn. Magn. Mater.*, 2015, **379**, 50–57.

6 P. L. Leng, M. G. Naseri, E. Saion, A. H. Shaari and M. A. Kamaruddin, *Adv. Nanopart.*, 2013, **2**, 378–383.

7 R. Rajesh Kanna, K. Sakthipandi, N. Lenin and E. James Jebaseelan Samuel, *J. Mater. Sci.: Mater. Electron.*, 2019, **30**, 4473–4486.

8 Somnath, I. Sharma, R. K. Kotnala, M. Singh, A. Kumar, P. Dhiman, V. P. Singh, K. Verma and G. Kumar, *J. Magn. Magn. Mater.*, 2017, **444**, 77.

9 T. J. Shinde, A. B. Gadkari and P. N. Vasambekar, *J. Alloys Compd.*, 2012, **513**, 80.

10 R. S. Yadav, J. Havlica, J. Masilko, L. Kalina, J. Wasserbauer, M. Hajduchova, V. Enev, I. Kuritka and Z. Kozakova, *J. Magn. Magn. Mater.*, 2016, **399**, 109.

11 X. Wu, W. Chen, W. Wu, J. Wu and Q. Wang, Improvement of the magnetic moment of Ni–Zn ferrites induced by substitution of Nd^{3+} ions for Fe^{3+} ions, *J. Magn. Magn. Mater.*, 2018, **453**, 246–253.

12 P. P. Naik, R. B. Tangsali, S. S. Meena and S. M. Yusuf, Influence of Rare Earth (Nd^{3+}) Doping on Structural and Magnetic Properties of Nanocrystalline Manganese–Zinc Ferrite, *Mater. Chem. Phys.*, 2017, **191**, 215–224.

13 G. S. Luo, W. P. Zhou, J. D. Li, *et al.*, The influence of Nd^{3+} ions doping on structural, dielectric and magnetic properties of Ni–Zn ferrites, *J. Mater. Sci.: Mater. Electron.*, 2017, **28**, 7259–7263.

14 T. Șașmaz Kuru, M. Kuru and S. Bağci, Structural, dielectric and humidity properties of Al–Ni–Zn ferrite prepared by co-precipitation method, *J. Alloys Compd.*, 2018, **753**, 483–490.

15 A. Ahmad, H. Bae, I. Rhee and S. Hong, *J. Magn. Magn. Mater.*, 2018, **447**, 42–47.

16 N. Sharma, P. Aghamkar, S. Kumar, M. Bansal, Anju and R. P. Tondon, *J. Magn. Magn. Mater.*, 2014, **369**, 162–167.

17 Z. A. Gilania, M. F. Warsic, M. N. Anjum, I. Shakird, S. Naseeme, S. Riaze and M. A. Khana, *J. Alloys Compd.*, 2015, **639**(5), 268–273.

18 R. A. Pawar, S. l. M. Patange and S. E. Shirsath, *RSC Adv.*, 2016, **6**, 76590.

19 J. Massoudi, M. Smari, K. Nouri, E. Dhahri, K. Khirouni, S. Bertaina, L. Bessais and E. K. Hlil, *RSC Adv.*, 2020, **10**, 34556–34580.

20 H. Javed, F. l. Iqbal, P. O. Agboola, M. A. Khan, M. F. Warsi and I. Shakir, Structural, electrical and magnetic parameters evaluation of nanocrystalline rare earth Nd^{3+} substituted nickel-zinc spinel ferrite particles, *Ceram. Int.*, 2019, **45**(8), 11125–11130.

21 H. S. Aziz, S. Rasheed, R. A. Khan, A. Rahim, J. Nisar, S. M. Shah, F. Iqbal and A. R. Khan, *RSC Adv.*, 2016, **6**, 6589.

22 E. F. Bertaut, Structures des boroferrites, *Acta Crystallogr.*, 1950, **3**, 473–474.

23 V. K. Lakhani, T. K. Pathak, N. H. Vasoya and K. B. Modi, *Solid State Sci.*, 2011, **13**, 539–547.

24 S. M. Patange, S. S. Desai, S. S. Meena, S. M. Yusuf and S. E. Shirsath, *RSC Adv.*, 2015, **5**(111), 91482–91492.

25 L. Wang, B. K. Rai and S. R. Mishra, Structural and magnetic study of Al^{3+} doped $Ni_{0.75}Zn_{0.25}Fe_2Al_xO_4$ nanoferrites, *Mater. Res. Bull.*, 2015, **65**, 183–194.

26 J. Massoudi, D. Bouekkeze, A. Bougoffa, K. Khirouni, E. Dhahri and L. Bessais, *Adv. Powder Technol.*, 2020, **31**, 4714–4730.

27 S. Yadav, I. Kuritka, J. Vilcakova, P. Urbanek, M. Machovsky, M. Masar and M. Holek, *J. Phys. Chem. Solids*, 2017, **110**, 87–99.

28 R. Qindeel and N. H. Alonizan, *Curr. Appl. Phys.*, 2018, **18**, 519–525.

29 Y. Gao, Z. Wang, J. Pei and H. Zhang, Structural, elastic, thermal and soft magnetic properties of Ni–Zn–Li ferrites, *J. Alloys Compd.*, 2019, **774**, 1233–1242.

30 N. Amri, M. Nasri, M. Triki and E. Dhahri, Synthesis and characterization of $(1 - x)(La_{0.6}Ca_{0.4}MnO_3)/x(Sb_2O_3)$ ceramic composites, *Phase Transitions*, 2018, **92**, 52–64.

31 G. Kumar, R. K. Kotnal, J. Shah, V. Kumar, A. Kumar, P. Dhiman and M. Singh, *Phys. Chem. Chem. Phys.*, 2017, **19**, 16669.

32 C. Murugesan and G. Chandrasekaran, *RSC Adv.*, 2015, **5**, 73714–73725.

33 Somnath, I. Sharma, R. K. Kotnala, M. Singh, A. Kumar, P. Dhiman, V. P. Singh, K. Verma and G. Kumar, Structural, magnetic and Mössbauer studies of Nd-doped Mg–Mn ferrite nanoparticles, *J. Magn. Magn. Mater.*, 2017, **444**, 77–86.

34 S. I. Ahmad, S. A. Ansari and D. R. Kumar, *Mater. Chem. Phys.*, 2018, **208**, 248–257.

35 D. Bouokkeze, J. Massoudi, W. Hzez, M. Smari, A. Bougoffa, K. Khirouni, E. Dhahri and L. Bessais, *RSC Adv.*, 2019, **9**, 40940.

36 E. R. Kumar, C. Srinivas, M. S. Seehra, M. Deepty, I. Pradeep, A. S. Kamzin, M. V. K. Mehar and N. K. Mohan, *Sens. Actuators, A*, 2018, **279**, 10–16.

37 A. Javed, T. Szumiata, A. Sarwar and T. Fatima, Structure and Mössbauer spectroscopy studies of $Ni_{0.5}Zn_{0.5}Nd_xFe_{2-x}O_4$ $(0.00 \leq x \leq 0.10)$ ferrites, *Mater. Chem. Phys.*, 2018, **221**, 99–107.

38 R. S. Yadav, J. Havlica, J. Masilko, L. Kalina, J. Wasserbauer, M. Hajdúchová, V. Enev, I. Kuřitka and Z. Kožáková, *J. Magn. Magn. Mater.*, 2016, **399**, 109–117.

39 M. K. Kokare, N. A. Jadhav, Y. Kumar, K. M. Jadhav and S. M. Rathod, Effect of Nd^{3+} doping on structural and magnetic properties of $Ni_{0.5}Co_{0.5}Fe_2O_4$ nanocrystalline ferrites synthesized by sol–gel auto combustion method, *J. Alloys Compd.*, 2018, **748**, 1053–1061.

40 A. Bajorek, C. Berger, M. Dulski, P. Łopadczak, M. Zubko, K. Prusik, M. Wojtyniak, A. Chrobak, F. Grasset and N. Randrianantoandro, Microstructural and magnetic characterization of $Ni_{0.5}Zn_{0.5}Fe_2O_4$ ferrite nanoparticles, *J. Phys. Chem. Solids*, 2019, **129**, 1–21.

41 M. M. Naik, H. S. B. Naik, G. Nagaraju, M. Vinuth, K. Vinu and S. K. Rashmi, *J. Mater. Sci.: Mater. Electron.*, 2018, **29**(23), 20395–20414.

42 S. A. Mazen, S. F. Mansour, E. Dhahri, H. M. Zaki and T. A. Elmosalami, *J. Alloys Compd.*, 2009, **470**, 294.

43 J. P. Singh, R. C. Srivastava, H. M. Agrawal and R. Kumar, *J. Raman Spectrosc.*, 2011, **42**, 1510.

44 M. Virumbrales-del Olmo, A. Delgado-Cabello, A. Andrada-Chacón, J. Sánchez-Benítez, E. Urones-Garrote, V. Blanco-Gutiérrez, M. J. Torralvo and R. Sáez-Puchea, *Phys. Chem. Chem. Phys.*, 2017, **19**, 8363–8837.

45 S. G. Kakade, R. C. Kambale, C. V. Ramanna and Y. D. Kolekar, *RSC Adv.*, 2016, **6**, 33308–33317.

46 M. A. Dar, K. Majid, M. H. Najar, R. K. Kotnala, J. Shah, S. K. Dhawan and M. Farukh, *Phys. Chem. Chem. Phys.*, 2017, **9**, 10629.

47 L. Néel, *C. R. Hebd. Seances Acad. Sci.*, 1950, **230**, 375–377.

48 F. Saida, H. Harzali, A. Marzouki, A. Mgaidi, A. Megriche and J. Tun, *Chem. Sci.*, 2017, **19**, 26–31.

49 M. Jeddi, H. Gharsallah, M. Bejar, M. Bekri, E. Dhahri and E. K. Hlil, *RSC Adv.*, 2018, **8**, 943.

50 M. Nasri, M. Triki, E. Dhahri, M. Hussein, P. Lachkar and E. K. Hlil, *Phys. Rev. B: Condens. Matter Mater. Phys.*, 2013, **408**, 104.

51 B. Martinez, V. Laukhin, J. Fontcuberta, L. Pinsard and A. Revcolevschi, *Phys. Rev. B: Condens. Matter Mater. Phys.*, 2002, **66**, 054436.

52 S. G. Gawas, S. S. Meena, P. Bhatt and V. M. S. Verenkar, Nanoscale-driven structural changes and associated superparamagnetism in magnetically diluted Ni–Zn ferrites, *Mater. Chem. Front.*, 2018, **2**(2), 300–312.

53 F. Saffari, P. Kameli, M. Rahimi, H. Ahmadvand and H. Salamati, *Ceram. Int.*, 2015, **41**, 7352–7358.

54 Somnath, I. Sharma, R. K. Kotnala, M. Singh, A. Kumar, P. Dhiman, V. P. Singh, K. Verma and G. Kumar, *J. Magn. Magn. Mater.*, 2017, **444**, 77–86.

55 R. H. Kodama, A. E. Berkowitz, J. E. J. McNiff and S. Foner, *Phys. Rev. Lett.*, 1996, **77**, 394.

56 A. Munir, F. Ahmed, M. Saqib and M. Anis-ur-Rehman, *J. Magn. Magn. Mater.*, 2016, **397**, 188–197.

57 H. El Moussaoui, T. Mahfoud, M. Ben Ali, Z. Mahhouti, R. Masrour, M. Hamedoun, E. K. Hlil and A. Benyoussef, *Mater. Lett.*, 2016, **171**, 142–145.

58 R. S. Pandav, R. P. Patil, S. S. Chavan, I. S. Mulla and P. P. Hankare, *J. Magn. Magn. Mater.*, 2016, **417**, 407–412.

59 K. K. Bamzai, G. Kour, B. Kaur and S. D. Kulkarni, *J. Magn. Magn. Mater.*, 2013, **327**, 159–166.

60 S. I. Ahmad, S. A. Ansari and D. R. Kumar, *Mater. Chem. Phys.*, 2018, **208**, 248–257.

61 M. Maria, L. Sonia, S. Anand, V. M. Vinosel, M. A. Janifer, S. Pauline and A. Manikandan, *J. Magn. Magn. Mater.*, 2018, **466**, 238–251.

62 S. Thankachan, B. P. Jacob, S. Xavier and E. M. Mohammed, *Phys. Scr.*, 2013, **87**(7), 025701.

63 J. Massoudi, M. Smari, K. Khirouni, E. Dhahri and L. Bessaisd, *J. Magn. Magn. Mater.*, 2021, **528**, 167806.

64 M. N. Akhtar, M. Babar, S. Qamar, Z. ur-Rehman and M. A. Khan, *Ceram. Int.*, 2019, **45**, 10187–10195.

65 M. N. Akhtar, M. Saleem and M. A. Khan, *J. Phys. Chem. Solids*, 2018, **123**, 260–265.